A Data-efficient Multiobjective Machine Learning Method For 3D-printed Architected Materials Design

Anonymous Author(s)
Affiliation
Address
email

Abstract

Architected materials that consist of multiple subelements arranged in particular orders can demonstrate a much broader range of properties than their constituent materials. However, the rational design of these materials generally relies on experts' prior knowledge and requires painstaking effort. Here, we present a data efficient method for the multiproperty optimization of 3D-printed architected materials utilizing a machine learning (ML) cycle consisting of the finite element method (FEM) and 3D neural networks. Specifically, we applied our method to orthopedic implant design. Compared to expert designs, our experience-free method designed microscale heterogeneous architectures with a biocompatible elastic modulus and higher strength. Furthermore, inspired by the knowledge learned by the neural networks, we developed machine-human synergy, adapting the ML-designed architecture to fix a macroscale, irregularly shaped animal bone defect. Such adaptation exhibits 20% higher experimental load-bearing capacity than the expert design. Thus, our method opens a new paradigm for the fast and intelligent design of architected materials with tailored mechanical, physical, and chemical properties.

1 Introduction

Architected materials are one of the most widely adopted engineering materials. Due to their excellent mechanical performance and adaptable properties, architected materials are very popular in many fields, such as those of light-weight structures [1, 2, 3], acoustics [4], battery electrodes [5], electromagnetics [6], and tissue engineering [7, 8]. Moreover, recent progress in 3D printing has further enabled the customized and inexpensive fabrication of complex material geometries.

Despite the broad applicability and immense potential of architected materials, designing them is particularly difficult. The traditional design method generally relies on numerical simulation, theoretical analysis, and topology optimization. These undertakings are usually exhausting and time-consuming, and the performance of resultant designs highly depends on the designer's professional knowledge and their initial guesses [9, 10]. Recently, machine learning (ML) has merged as a promising technique to circumvent this problem and find the optimal solution without any prior knowledge requirements [11, 12, 13]. However, the proposed ML methods require massive amounts of simulation data and mainly aim to solve 2D-structure-related problems. Efforts toward solving 3D real-world problems are often obfuscated by the lack of credible data sources, the enormity of design space and multidimensional complex patterns. Moreover, real-world design problems usually require multiobjective property optimization under possible external constraints, yet the current ML methods mostly attempt to solve unconstrained single-objective optimization problems.

Therefore, we propose an ML approach for data-efficient, multiobjective architected material design. As demonstrated in Fig. 1(A to D), our approach consists of three main parts: 1) generative architec-

Submitted to 36th Conference on Neural Information Processing Systems (NeurIPS 2022). Do not distribute.

ture design (GAD). In this step, GAD leverages the encoder-decoder neural network (autoencoder) to generate architecture sets with unknown properties. Until recently, experimental discovery of architected materials has relied on simple surrogate models and Bayesian optimization, which are limited to low-dimensional data, thus showing property improvements only after many iterations [14]. Unlike the Bayesian methods, the autoencoder learns an effective representation of the high-dimensional data in an unsupervised manner, which converts the exploration in a high-dimensional design space into a lower one. This method has been proven to be a revolutionary technique in materials discovery [15, 16]. However, to the best of our knowledge, this is the first time that a 3D convolutional autoencoder(3D-CAE) has been applied to 3D structure generation with high dimensionality (for details see Section A.3). 2) Multi-objective Active Learning Loop (MALL). MALL evaluates the generated dataset and searches for the high-performance architecture by recursively querying the finite element method (FEM). Active learning describes a specialized ML algorithm that interactively queries an information source such that the algorithm identifies high-value data with fewer labeled data than typical ML [17, 18]. Such data efficiency is highly desirable since constructing a large dataset with known properties is very difficult both computationally and experimentally. 3) 3D printing and testing. Finally, we fabricate the ML-designed architected materials via a specialized 3D printing technique (laser powder bed fusion) and experimentally verify the corresponding mechanical properties. We call the overall method ’GAD-MALL’.

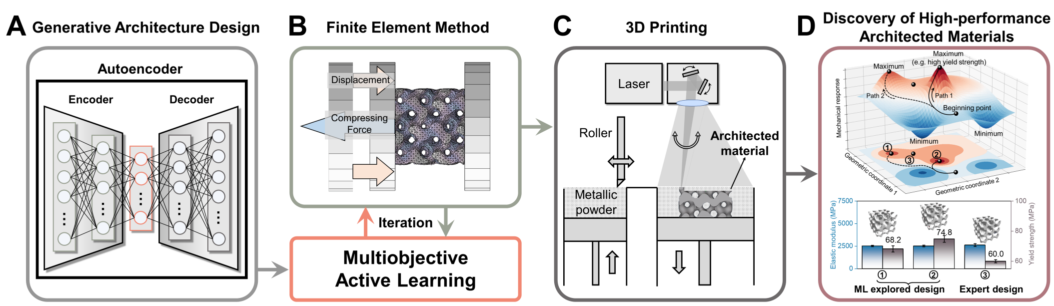

Figure 1: **An overview of the proposed workflow (GAD-MALL).** (**A**) The neural network proposes candidates with unknown properties. (**B**) The ML algorithm interactively queries the FEM to propose new designs. (**C**) The 3D printing technique fabricates the proposed architectural design. (**D**) GAD-MALL explores the design landscape of architected materials and discovers various high-performance architected materials.

2 Results

2.1 Multiobjective active learning algorithm

We applied the GAD-MALL approach to a multiproperty optimization problem with clinical importance - bone grafting implants. Bone is a typical architected material primarily consisting of cortical and cancellous parts, with elastic modulus (E) ranging from 0.03 to 30 GPa depending on the bone mineral density and varying according to age, sex, and race [19]. Although bone can repair itself, a bone defect of a critical size necessitates a grafting implant to support the load and induce bone growth. Metals are the first choice for bone implant materials due to their excellent mechanical properties. However, the E of the existing metal bulk materials is much greater than that of the bones (i.e., titanium – 100 GPa; iron - 200 GPa, etc.), which results in the stress shielding effect and impedes the recovery of the bone [20]. One effective solution is introducing a 3D-printed scaffold architecture to lower the E. The geometrical shape and mechanical properties of the scaffold should be comparable to those of the individual defective bone to provide reliable structural support and smooth stress conduction. Fig. 2(A) demonstrates a typical mechanical response of the scaffold. The slope of the linear section of the curve indicates E, which measures a material’s ability to resist external stress before being deformed permanently, and the yield point with 0.2% strain represents the yield strength (Y), which quantifies the maximum resistance before the onset of nonreversible deformation. Overall, the design tasks are multiobjective: First, the E of the replacement scaffold must match that of the bone. Second, The Y must be as high as possible to sustain bone movement. In addition, the overall weight of the scaffold should not go beyond a certain threshold since a minimum usage is always required considering long-term biosafety.

A cubic scaffold and its 3D-printed experimental counterpart are shown in inlets of Fig. 2(A). To balance complexity and computing efficiency, we adopted the $3 \times 3 \times 3$ cubic arrangement of the gyroid unit for the optimization task (see Methods for the structure generation). The gyroid geometry is categorized in the triply periodic minimal surfaces (TPMS) family - it is an ideal porous structure for bone scaffolds due to its high interconnectivity, smooth surface, and mathematically adjustable geometrical attributes [21, 22]. Instead of a uniform-sized array of periodic subunits (the expert design), the ML design introduced heterogeneity: GAD-MALL adjusts the size of the gyroid unit (porosity) within the scaffold, resulting in a geometrical alteration that modulates the overall mechanical properties.

Fig. 2(B) shows the models of the 3D convolutional neural network (3D-CNN) for the E and Y prediction. The 3D-CNN was designated for volumetric data representation learning [23, 24]. It included three main components: input, convolution, and output layers. At the input layer, the scaffold structure was voxelized into $60 \times 60 \times 60$ pixels. A pixel can be in either the solid (1) or void (0) phase in the scaffold. The convolution layers consisted of a series of 3D convolution kernels that extracted high-level information about the scaffold, and the output layer provided the final prediction. Finally, a training dataset was prepared using the protocol described in the Methods.

Fig. 2(C) illustrates the 3D-CAE with a typical two-neural network model, an encoder and a decoder. Notably, the original $60 \times 60 \times 60$ scaffold structure was not used because the decoder could not reliably recover the original gyroid geometry due to the nonzero reconstruction error. However, thanks to the high mathematical controllability of gyroid geometry, we circumvented this problem by adopting the porosity matrix, a 3D matrix representation ($3 \times 3 \times 3$) that uniquely determines the overall geometry through Gyroid equations (see Methods). It measures the relative density (positive scalars) rather than the actual shape of the gyroid subunits, thereby allowing nonzero reconstruction errors. The encoder $q_\phi(z|x)$ with parameters ϕ compressed the porosity matrix into a hidden feature representation (8-dimension) using the neural encoder. Then the decoder $q_\varphi(x|z)$with parameters φ reconstructed the output from the 8-dimension hidden features. A lower-dimension (e.g., 4-dimension) latent space was shown to suffer from high reconstruction error, while a higher-dimension (e.g., 16-dimension) doubled the search space without a sufficient increase in reconstruction accuracy. Ultimately, 8-dimensional represented a balance between loss and efficiency (Section A.2 and Fig. 7).

Fig. 2(D) shows the primary steps of the MALL workflow, which comprised three steps. First, the scaffold generation was formulated as a process of sampling and reconstruction from the latent representation z. The sampling process required the latent representation to be modeled as a continuous probabilistic distribution (Section A.2). Secondly, the decoder $q_\phi(x|z)$ reconstructed the porosity matrices from the sampled latent points, which were then converted to their original shapes in Cartesian space. The scaffold selection method was a variant of the epsilon-greedy search: in each sampling iteration, we sampled 2000 data points and selected those whose 3D-CNN-predicted E met the target and whose 3D-CNN-predicted Y exceeded the best data point in the current dataset, with a chance of epsilon (5%) chances that the lower ones were chosen. The selected data points would still be rejected if their weights were 15% higher than preset criteria. Such a search method generally had a higher success rate than the Edisonian approach, which hinged on a trial-and-error search [25]. Last, the FEM calculated the E and Y of the queried scaffolds, and the results would augment the dataset, from which the 3D-CNNs were re-trained for the following active learning round. The workflow stopped when all the preset criteria were met.

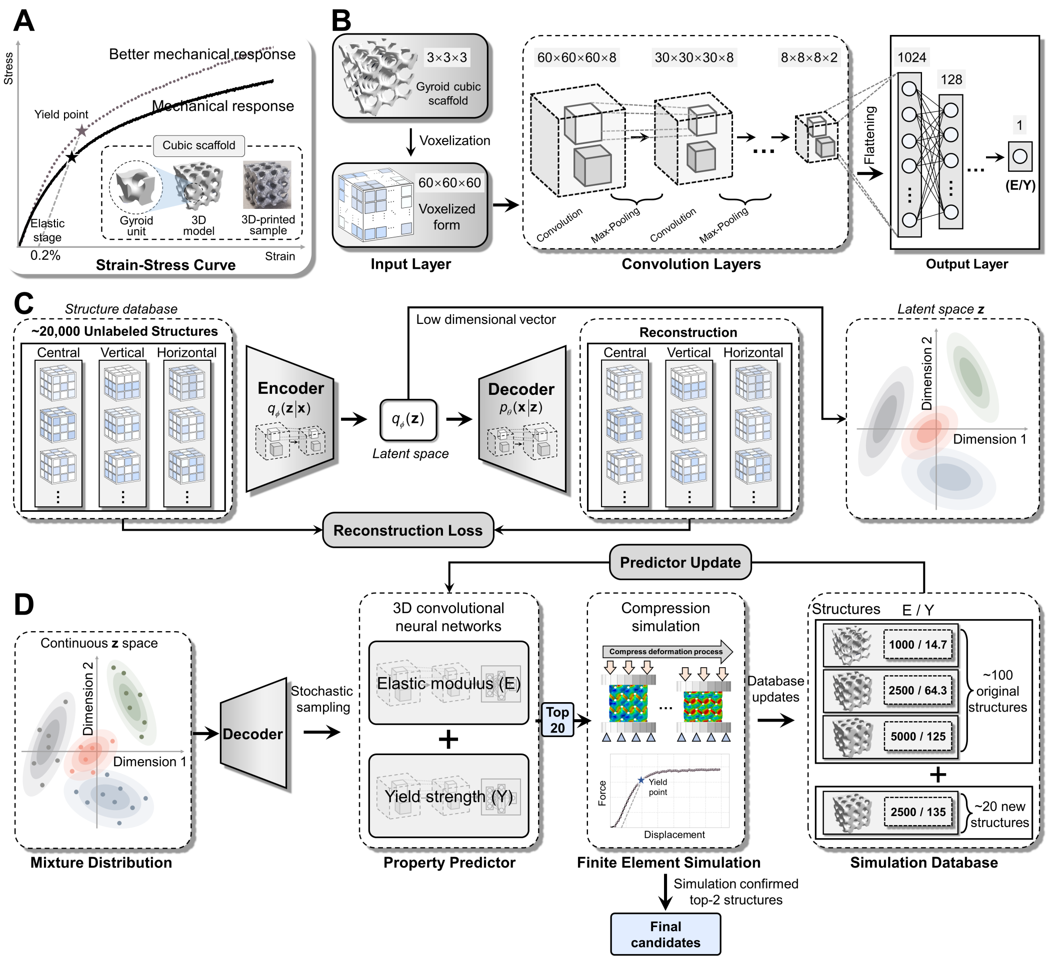

Figure 2: **The workflow of multiobjective active learning.** (**A**) The task was to design scaffolds with a better mechanical response - fixed E and maximized Y. (**B**) The 3D-CNN models for predicting E and Y. (**C**) The generative model for targeted scaffold generation. The encoder q_ϕ (z|x) with parameters ϕ took the scaffold porosity matrix as input and the decoder p_θ (x|z) with parameters θ could act as a generator for proposing new scaffolds based on the learned latent z representation. (**D**) The MALL for the high-performance scaffold discovery. First, the sampling algorithm sampled new data points from the latent z representation. Second, the decoder reconstructed the corresponding scaffolds so that the 3D-CNNs could infer their mechanical properties. Third, the most suitable candidates were selected based on the predicted E and Y. Finally, the strain-stress curves of the selected scaffolds were calculated by the FEM. New data were either fed back to the dataset or 3D-printed for further experiments.

2.2 Applications to orthopedic implants

The properties of the architected materials are determined by both the scaffold architecture and the constituent materials. For orthopedic implants, the orthopedic materials Ti6Al4V (Ti) and pure zinc (Zn) were used as the constituent materials. Ti alloy is bioinert in human bodies and has been the de facto choice for 3D-printed orthopedic implants, achieving successful clinical application to repairing bone defects. Biodegradable Zn provides an alternative option to bioinert materials and is regarded as promising for addressing the clinical concerns associated with permanent existence and secondary surgery [26]. Such features are especially desirable for bone regeneration. As both materials are worthy of investigation, to demonstrate the effectiveness and general applicability of the GAD-MALL framework, we designed two optimization tasks for both constituent materials and applied the learned design principle to the real bone replacement architecture. Specifically, the Ti alloy scaffolds were assigned a high E while the pure Zn scaffolds had a low E, indicating different clinical needs based on the constituent materials. In addition, two tasks were given different initial data distributions to demonstrate that GAD-MALL can work under different initial conditions. Notably, all tasks were completed in one week with the current hardware setup, as tasks in the clinical scene are usually time-constrained. In the following section, we begin with the Ti cubic scaffolds.

2.2.1 A data-efficient route toward high-performance structure

To mimic the mechanical behavior of trabecular and compact bones, the task was to design high-Y scaffolds with E = 2500 MPa and 5000 MPa (E2500 and E5000). The expert-designed uniform scaffolds at E = 2500 MPa and 5000 MPa set the 'golden criteria' for the mechanical performance of the scaffolds. GAD-MALL stopped if the Y of the designed scaffolds significantly surpassed the golden criteria (termed the 'treasure' scaffold) or the learning process showed no further progress. The initially labeled dataset was composed of merely 75 data points (the simulation took ca. 7 days, hardware specified in the A.1 section). Fig. 3B shows that the scaffolds had been precisely manufactured - the cross-sections of the microcomputed tomography (Micro-CT) of the scaffolds largely overlapped (92.2%) with that of the designs. Fig. 3(A and C) demonstrates the good performance of 3D-CNNs on the test dataset (uniformly sampled from the labeled dataset) in the 1st round and last round, in which both 3D-CNNs demonstrate high accuracy (R^2 ratio 0.92). A more detailed performance evaluation can be found in Section A.2.

Fig. 3(E) shows the overall data distribution in terms of E and Y with the treasure scaffolds indicated by blue stars. Each active learning iteration is characterized by colored eclipses. Fig. 3(D and F) demonstrates two distinct exploration paths for two different tasks. The E2500 exploration path shows a steady upward trend, and GAD-MALL quickly discovered the treasure scaffolds at the 3rd and 5th rounds with more than a 30% increase in Y. However, the E5000 task was more complicated - the learning process experienced a downhill before it recovered and found the treasure scaffolds. Specifically, the batches from 1st to 3rd round either fell out of the target E region or had inferior Y values. The 4th-round batch finally hit the target of E; albeit Y was not notably better than that of the expert designs. Finally, the treasure scaffolds were discovered on the 5 and 6th rounds. This oscillatory trend is likely due to the sparsity of data within this range (with only two initial data points available). The computed mechanical properties of the resultant designs are tabulated in Section A.5.

The experiments confirmed the discovery - the ML-designed scaffolds (A1-A4) showed better performance than the expert-designed scaffolds (H1 and H2, Fig.3(G)). For example, the experimental strain-stress curves of the A1 and H1 scaffold are also displayed in the inset (full detail in Section A.5). To understand the ML design, we further analyzed the ML-designed scaffold by extracting the corresponding regression activation map (RAM) and performing FEM mechanical analysis. As an illustrative example, we applied the RAM to the Y-predicting 3D-CNN to reveal the driving mechanism behind the high Y of the A1 scaffold. RAM is a variant of a classification activation map, that extracts the last convolutional layer to visualize the discriminative regions used by a 3D-CNN to predict the output [27]. In this case, the RAM highlights the scaffold's spatial characteristics that correlate to its mechanical strength, identifying the regions that contribute to the enhancement of strength. Fig. 3(H) demonstrates the A1 scaffold geometrical structure, the corresponding porosity matrix and the RAM. The RAM implies that the 'attention' distribution extracted from the 3D-CNN resembled a heterogeneous 'face-centered' lattice. Indeed, a closer look at the A1 scaffold revealed that the gyroid units at each face center of the scaffold show a minimal porosity (0.3). This observation indicates that instead of uniformity, a heterogeneous scaffold with more materials distributed at the face centers could significantly enhance the strength. Moreover, from a macroscopic point of view, the strength of a typical porous structure can be approximated by the Gibson-Ashby equation [28]:

$$Y \;\; C(1-p)^{\alpha} Y_0 \tag{1}$$

where Y_0 stands for the strength of the constituent material, C represents a geometry-related parameter, p is the porosity of the unit, and the exponent α relates to the deformation behavior of the structure. According to the FEM calculated data in Table S4, we fitted the curve of strength Y as a function of p for ML and expert-designed scaffolds and found: a_{ML} 2.11, a_{ED} 1.86, C_{ML} 0.84 and C_{ED} 0.64, in which ED stands for expert design.

The ML-designed scaffold had a larger a and C than the expert design. Generally, increasing the mechanical anisotropy of a porous structure leads to an increase in the exponential factor a; while an increase in parameter C can be found in the material distribution in favor of the load direction [29].

Microscopically, FEM analysis confirmed the above observation. Fig. 3(I) shows the distribution of von Mises stress and hydrostatic pressure of the A1 and H1 scaffolds. Compared with the H1 scaffold, the A1 scaffold endures a much weaker effect of stress concentration; moreover, more struts of the A1 scaffolds are compressed rather than stretched. The ML model preferentially places more materials on the face center of the scaffolds, which optimizes the stress distribution and improves the structural strength with increasing limited mass. Hence, GAD-MALL was able to find the optimal architectures by efficiently learning from a few initial data points.

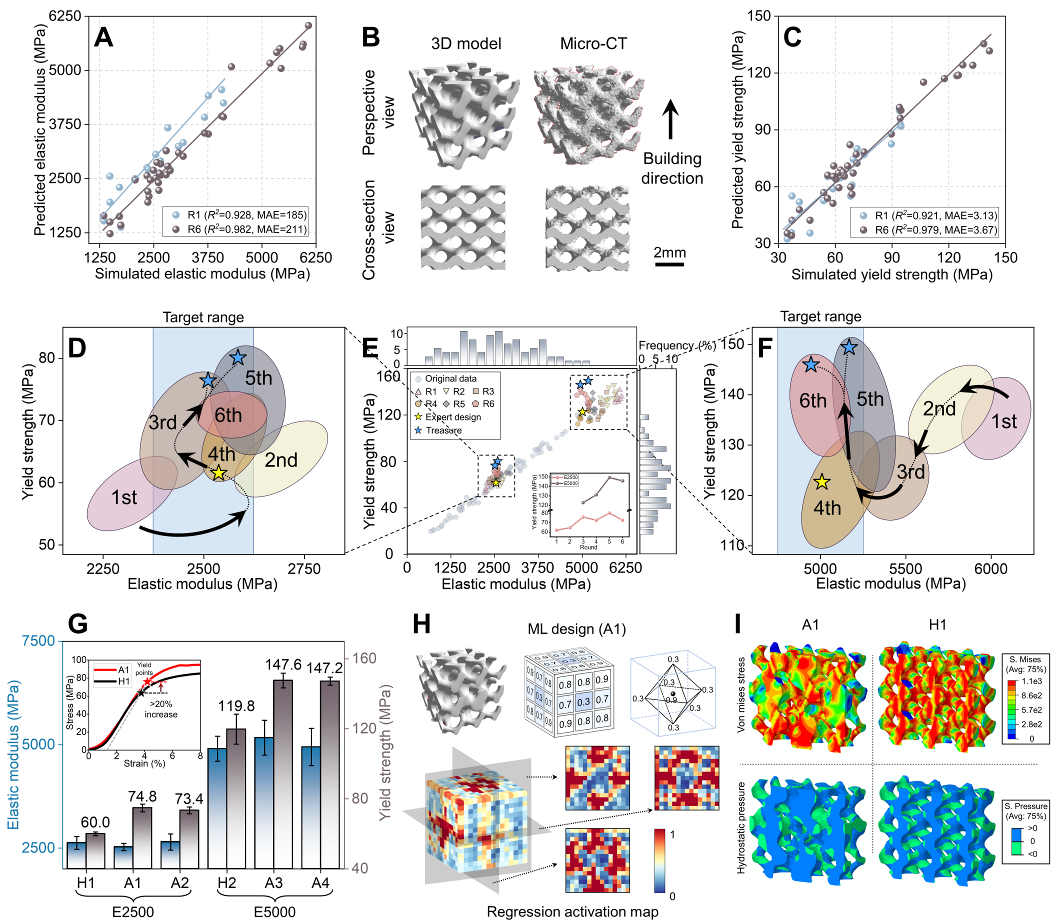

Figure 3: **Data-efficient learning of high-performance scaffolds.** (**A** and **C**) The regression plots (1st and last rounds of active learning) of the 3D-CNNs for E and Y. Both 3D-CNNs demonstrate excellent accuracy on the testing set, showing low mean absolute error (MAE) and high R^2 ratio. (**B**) Micro-CT shows that the designated scaffolds were accurately manufactured. (**D** to **F**) The overall data distribution in terms of the E-Y plot. The colored eclipses indicate the area covered by 6 rounds of active learning data, and the learning paths are marked by black arrows. (**G**) Comparison of the experimental E and Y between ML-designed (A1, A2 for E2500 and A3, A4 for E5000) and expert-designed (H1 for E2500, H2 for E5000) scaffolds. The Y of the ML-designed scaffolds was obviously higher than that of the expert designs. (**H**) The upper figures show the mathematical model of the A1 scaffold and its porosity matrix. The lower figures contain the 3D view and three cross-section views of the RAM. The RAM reveals a 'face-centered' lattice in the A1 scaffold, implying its prominent role in enhancing the Y. This face-centered lattice is displayed in the upper right part of the figure. (**I**) Numerical compression analysis. Here we show the y-z cross-sections of A1 and H1 scaffolds in terms of von Mises stress and hydrostatic pressure under 10% deformation.

2.2.2 Learning without prior data at target range

To demonstrate the robustness of the GAD-MALL approach, we designed a learning task by which GAD-MALL found the appropriate scaffolds 'from scratch' - the initial Zn dataset did not contain any prior data points in the target range by design. The task of this section was to design high-Y scaffolds at E = 500 MPa and 1000 MPa (E500 and E1000) targeting to replacement of cancellous bone. Again, the expert-designed scaffolds at E = 500 MPa and 1000 MPa set the 'golden criteria'.

Fig. 4(A to C) illustrate the E-Y distribution of the initial data (marked in gray) and the results from each active learning round characterized by colored eclipses. Fig. 4(B) demonstrates that the GAD-MALL exploration paths of the missing data were complicated, exhibiting back-and-forth trends. For the E500 task, the E distribution of the 1st round shows a significant standard deviation. It is noteworthy that some scaffolds from the 1st round had already reached the target E $\approx$ 500 MPa. The 2nd round shows improvement - the overall standard deviation was significantly reduced (from 52 to 19 MPa). While all scaffolds' E located at approximately 500 MPa, the Y values were still 30% less than the golden criteria. In the following rounds, the exploration path reached a plateau, and the selected candidates were slightly better than the golden criteria (14.8 MPa). The E500 task was terminated after the 5th round since no further progress was observed (see inset). The detailed results of each learning round are described in Section A.2.

On the other hand, GAD-MALL excelled at the E1000 tasks, outperforming the golden criteria by a large margin. More specifically, the 1st round already showed promising results, in which all scaffolds exhibited the targeted E, although with slightly worse Y ($\approx$10%). The subsequent round witnessed a significant decrease in porosity (Section A.2), which in turn remarkably enhanced Y. However, the reduced porosity resulted in another problem - the E increased to 1200 $\sim$ 1400 MPa. GAD-MALL incorporated this knowledge into the database in the subsequent learning process. Eventually, the average porosity increased, and the treasure scaffolds were discovered in the 3 and 4th rounds. The entire learning process took approximately 9 days, and the mechanical properties of the resultant designs are tabulated in Section A.5.

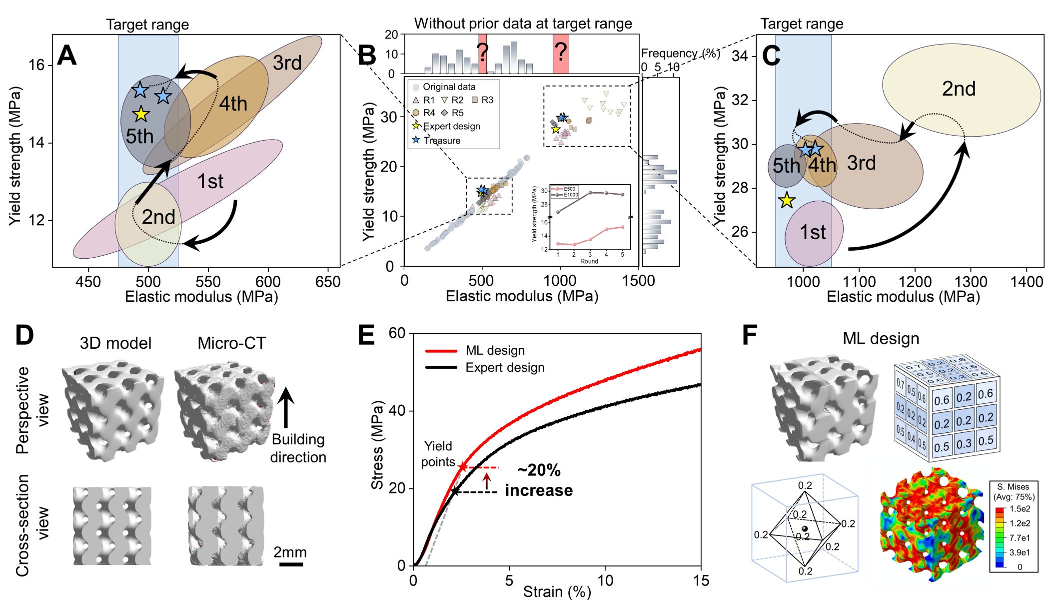

Figure 4: **Learning without prior data at the target range.** (**A** to **C**) The E-Y distribution. The colored eclipses indicate the area covered by 5 rounds of active learning data and black arrows specify the learning paths. (**D**) Micro-CT shows that the designated Zn scaffolds were manufactured with good precision. (**E**) The experimental strain-stress curves of the ML and expert-designed scaffolds. The ML design yielded a 20% increase in Y. (**F**) The porosity of the ML-designed scaffold reached the lower limit (0.2) at the face centers and the center of the scaffold. Similar to the ML-designed Ti scaffold, the compression analysis shows that the low-porosity units of the ML-designed Zn scaffold have higher stress concentrations.

Fig. 4(D) illustrates the model and micro-CT of an exemplary ML-designed scaffold (more ML designs see Section A.5). From the cross-section view, the model and manufactured sample were shown to agree with each other. The ML-designed scaffolds were manufactured, and their mechanical properties were measured experimentally (Fig. 4(E)). The ML design had a significant performance advantage over the expert design, whose Y (26.4 $\pm$ 0.7 MPa) exceeded the golden criteria (21.7 $\pm$ 1.8 MPa) by a large margin of 21.6%, with a slightly lower porosity (full detail in Section A.5). As the E and Y of the bulk Zn were less than those of the Ti alloy, the Zn scaffold still had a lower porosity even though the target E was only 1000 MPa. Similar to the Ti scaffold, the FEM analysis in Fig. 4(F) shows that the low-porosity face-centered units in the ML-designed scaffold had higher stress concentrations, leading to enhanced strength. Since the face-centered and the central unit of the Zn scaffold had reached the lower limit (porosity = 0.2) and the excess weight was allocated to the central and the ridge center unit of the cubic scaffold, the E of the scaffold did not hit the targeted E range (E = 1000 $\pm$ 100 MPa). Thus, the central and ridge-center units promoted E to the target range, without decreasing Y.

In this task, we showcased that GAD-MALL was able to find the optimal architecture even when the initial data distribution and the constituent material are considerably different from the previous section. Such robustness is highly desirable since clinical situations can be variable-the patient data (target material and mechanical range) are often unknown beforehand and the initial data can have various distributions.

2.3 ML-inspired anatomic bone implants

Most real-world bone implants require scaffolds in anatomical shapes that fit to the defective bone. Fig. 5(A and B) shows a large, irregular-shaped bone defect in a New Zealand rabbit model animal model - a defect of critical size (30 mm) occurred in the middle part of the tibia. Fig. 5(C) shows the 3D shape of the tibia, which was acquired through micro-CT scanning. It is difficult and time-consuming to find the optimal scaffold architecture to fit the shape, whether by experimental or by numerical trials, since there are many possible choices. Here, we demonstrate how a machine-learned design principle can be readily adapted to a clinical scene through a facile machine-human design workflow.

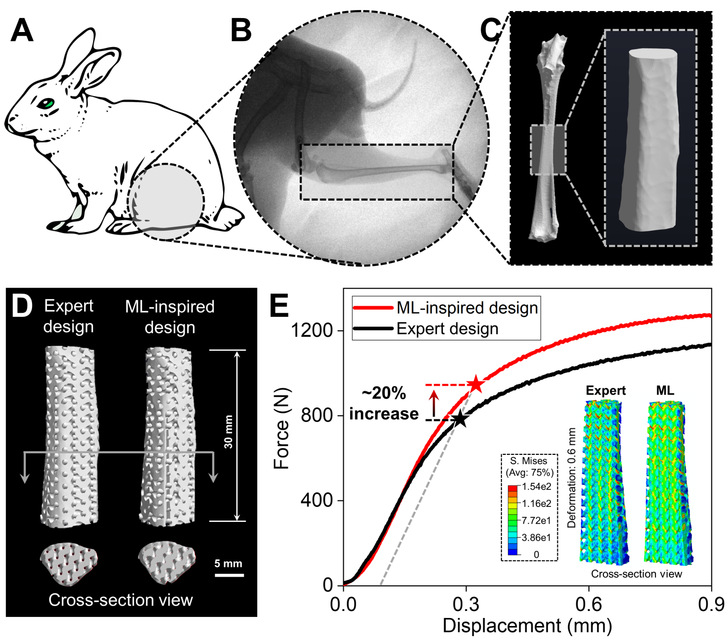

Figure 5: **Anatomic bone fixation with ML design.** (**A** and **B**) A 30 mm bone defect in the middle part of the tibia in a New Zealand rabbit. (**C**) Micro-CT of the tibia. (**D**) Cross-sectional view of ML-inspired and expert design. (**E**) Experimental displacement-force curves of the ML-inspired design versus expert design. The inset shows the cross-sections of von Mises stress under 0.6 mm deformation for both designs.

Concretely, to use the ML-designed cubic scaffold for a larger implant for large, irregularly shaped bone defect fixation, our workflow constituted the following two steps: 1) Using the ML-designed cubic scaffold as the basic unit, we manually created a cuboid of $3 \times 3 \times 9$ units with width, length, and height of 18 mm, 18 mm, and 54 mm respectively. 2) Subsequently, we caved out an irregularly shaped scaffold from the interior of the cuboid that matched the bone shape (shown in Fig. 5(D)). The detailed workflow is described in Section A.6. The resultant implant design and its 3D-printed counterpart are illustrated in the inset of Fig. 5(E). The mechanical behaviors at the macroscale could be characterized by the displacement-force curves in Fig. 5(E), which confirmed that the stiffness of expert-designed and ML-inspired implants were almost the same, while the ML-inspired implant's load-bearing capacity (indicated by stars) was considerably higher (20%). The von Mises stress distribution, given in the inset of Fig. 5(E), showed that the overall stress (under 6% deformation) of ML-inspired design was considerably higher than that of the expert design. With the same bone shape and deformation, the higher inner stress of the ML-inspired design indicated stronger support of the bone implant. Therefore, the strengthening effect of ML-learned face-centered lattice was accumulative; a large structure made up of many individual strengthened cubes still demonstrated better load-bearing capacity than the expert design of the same scale.

3 Discussion

This work demonstrates a multiobjective active learning approach for designing 3D-printed architected materials with generative models and 3D neural networks. With only 75 initial fine-tuned FEM simulation data points, our approach quickly discovered high-performance architected materials. Thus, by fusing high-precision simulation, ML, and 3D printing, our framework was developed into a powerful and robust tool that excels at complex multiobjective architecture optimization. It represents a data-efficient, intelligent method that requires no prior knowledge and can be readily adopted in wide-ranging architected materials applications. In this study, porosity is the only variable; in the future, our method can be extended to more advanced intelligent designs of geometrically complex metamaterials [30]. For example, one can either set new optimization objectives with the same algorithm (e.g., weight reduction, etc.) or introduce more architectural degrees of freedom such as the geometries of subunits to design 3D-printed materials with exotic architectures and customized properties. Furthermore, our framework provides interpretable patterns that bring new insights into the design philosophy of multidimensional architected materials. As a proof of concept, we demonstrated that ML-obtained knowledge from a relatively simple problem setting can be readily adapted to a complex, real-world scenario. Here, we developed a synergistic machine-human design methodology that uses machine-learned small-scale, regular structures as subunits to create large-scale, irregularly shaped architecture. In principle, such synergy can be extended to other types of architected materials. Overall, we anticipate that our methodology can be used for designing novel 3-D architectures where optimal responses to various stimuli are desirable, including mechanical, thermal, and chemical conditions or application requirements.

References

[1] Xiaoyan Li and Huajian Gao. Smaller and stronger. *Nature Materials*, 15(4):373–374, 2016. ISSN 1476-4660. doi: 10.1038/nmat4591. URL `https://doi.org/10.1038/nmat4591`.

[2] Ting Yang, Hongshun Chen, Zian Jia, Zhifei Deng, Liuni Chen, Emily M. Peterman, James C. Weaver, and Ling Li. A damage-tolerant, dual-scale, single-crystalline microlattice in the knobby starfish, <i>protoreaster nodosus</i>. *Science*, 375(6581):647–652, 2022. doi: 10.1126/science.abj9472. URL `https://www.science.org/doi/abs/10.1126/science.abj9472`.

[3] Minh-Son Pham, Chen Liu, Iain Todd, and Jedsada Lertthanasarn. Damage-tolerant architected materials inspired by crystal microstructure. *Nature*, 565(7739):305–311, 2019. ISSN 1476-4687. doi: 10.1038/s41586-018-0850-3. URL `https://doi.org/10.1038/s41586-018-0850-3`.

[4] Jensen Li, Lee Fok, Xiaobo Yin, Guy Bartal, and Xiang Zhang. Experimental demonstration of an acoustic magnifying hyperlens. *Nature Materials*, 8(12):931–934, 2009. ISSN 1476-4660. doi: 10.1038/nmat2561. URL `https://doi.org/10.1038/nmat2561`.

[5] T. A. Schaedler, A. J. Jacobsen, A. Torrents, A. E. Sorensen, J. Lian, J. R. Greer, L. Valdevit, and W. B. Carter. Ultralight metallic microlattices. *Science*, 334(6058):962–965, 2011. doi: 10.1126/science.1211649. URL `https://www.science.org/doi/abs/10.1126/science.1211649`.

[6] Xiaoxing Xia, Christopher M Spadaccini, and Julia R Greer. Responsive materials architected in space and time. *Nature Reviews Materials*, 2022. ISSN 2058-8437. doi: 10.1038/s41578-022-00450-z. URL `https://doi.org/10.1038/s41578-022-00450-z`.

[7] Anh-Vu Do, Behnoush Khorsand, Sean M Geary, and Aliasger K Salem. 3d printing of scaffolds for tissue regeneration applications. *Advanced healthcare materials*, 4(12):1742–1762, 2015.

[8] Meng Zhang, Rongcai Lin, Xin Wang, Jianmin Xue, Cuijun Deng, Chun Feng, Hui Zhuang, Jingge Ma, Chen Qin, Li Wan, Jiang Chang, and Chengtie Wu. 3d printing of haversian bone–mimicking scaffolds for multicellular delivery in bone regeneration. *Science Advances*, 6:eaaz6725, 7 2022. doi: 10.1126/sciadv.aaz6725. URL `https://doi.org/10.1126/sciadv.aaz6725`. doi: 10.1126/sciadv.aaz6725.

[9] Johan Christensen, Muamer Kadic, Oliver Kraft, and Martin Wegener. Vibrant times for mechanical metamaterials. *MRS Communications*, 5(3):453–462, 2015. doi: 10.1557/mrc.2015.51.

[10] Pai Wang, Filippo Casadei, Sicong Shan, James C. Weaver, and Katia Bertoldi. Harnessing buckling to design tunable locally resonant acoustic metamaterials. *Phys. Rev. Lett.*, 113:014301, Jul 2014. doi: 10.1103/PhysRevLett.113.014301. URL `https://link.aps.org/doi/10.1103/PhysRevLett.113.014301`.

[11] Yunwei Mao, Qi He, and Xuanhe Zhao. Designing complex architectured materials with generative adversarial networks. *Science Advances*, 6(17), 2020. ISSN 23752548. doi: 10.1126/sciadv.aaz4169.

[12] Chunping Ma, Zhiwei Zhang, Benjamin Luce, Simon Pusateri, Binglin Xie, Mohammad H Rafiei, and Nan Hu. Accelerated design and characterization of non-uniform cellular materials via a machine-learning based framework. *npj Computational Materials*, 6(1):40, 2020. ISSN 2057-3960. doi: 10.1038/s41524-020-0309-6. URL `https://doi.org/10.1038/s41524-020-0309-6`.

[13] Paul Z. Hanakata, Ekin D. Cubuk, David K. Campbell, and Harold S. Park. Accelerated search and design of stretchable graphene kirigami using machine learning. *Phys. Rev. Lett.*, 121:255304, Dec 2018. doi: 10.1103/PhysRevLett.121.255304. URL `https://link.aps.org/doi/10.1103/PhysRevLett.121.255304`.

[14] Dezhen Xue, Prasanna V. Balachandran, John Hogden, James Theiler, Deqing Xue, and Turab Lookman. Accelerated search for materials with targeted properties by adaptive design. *Nature Communications*, 7: 1–9, 2016. ISSN 20411723. doi: 10.1038/ncomms11241.

[15] Benjamin Sanchez-Lengeling and Alán Aspuru-Guzik. Inverse molecular design using machine learning: Generative models for matter engineering. *Science*, 361(6400):360–365, 2018. doi: 10.1126/science.aat2663. URL `https://www.science.org/doi/abs/10.1126/science.aat2663`.

[16] Ziyuan Rao, PoYen Tung, Ruiwen Xie, Ye Wei, Hongbin Zhang, Alberto Ferrari, T. P. C. Klaver, Fritz Körmann, Prithiv Thoudden Sukumar, Alisson Kwiatkowski da Silva, Yao Chen, Zhiming Li, Dirk Ponge, Jörg Neugebauer, Oliver Gutfleisch, Stefan Bauer, and Dierk Raabe. Machine learning-enabled high-entropy alloy discovery, 2022. URL `https://arxiv.org/abs/2202.13753`.

[17] Neil Rubens, Mehdi Elahi, Masashi Sugiyama, and Dain Kaplan. *Active Learning in Recommender Systems*, pages 809–846. Springer US, Boston, MA, 2015. ISBN 978-1-4899-7637-6. doi: 10.1007/978-1-4899-7637-6_24. URL `https://doi.org/10.1007/978-1-4899-7637-6_24`.

[18] Shubhomoy Das, Weng-Keen Wong, Thomas Dietterich, Alan Fern, and Andrew Emmott. Incorporating expert feedback into active anomaly discovery. In *2016 IEEE 16th International Conference on Data Mining (ICDM)*, pages 853–858, 2016. doi: 10.1109/ICDM.2016.0102.

[19] Xiaojian Wang, Shanqing Xu, Shiwei Zhou, Wei Xu, Martin Leary, Peter Choong, M. Qian, Milan Brandt, and Yi Min Xie. Topological design and additive manufacturing of porous metals for bone scaffolds and orthopaedic implants: A review. *Biomaterials*, 83:127–141, 2016. ISSN 0142-9612. doi: https://doi.org/10.1016/j.biomaterials.2016.01.012. URL `https://www.sciencedirect.com/science/article/pii/S0142961216000144`.

[20] Hongtao Yang, Bo Jia, Zechuan Zhang, Xinhua Qu, Guannan Li, Wenjiao Lin, Donghui Zhu, Kerong Dai, and Yufeng Zheng. Alloying design of biodegradable zinc as promising bone implants for load-bearing applications. *Nature Communications*, 11(1):401, 2020. ISSN 2041-1723. doi: 10.1038/s41467-019-14153-7. URL `https://doi.org/10.1038/s41467-019-14153-7`.

[21] Cécile M Bidan, Krishna P Kommareddy, Monika Rumpler, Philip Kollmannsberger, Peter Fratzl, and John W C Dunlop. Geometry as a factor for tissue growth: towards shape optimization of tissue engineering scaffolds. *Advanced healthcare materials*, 2(1):186–194, jan 2013. ISSN 2192-2640 (Print). doi: 10.1002/adhm.201200159.

[22] David Downing, Alistair Jones, Milan Brandt, and Martin Leary. Increased efficiency gyroid structures by tailored material distribution. *Materials & Design*, 197:109096, 2021. ISSN 0264-1275. doi: https://doi.org/10.1016/j.matdes.2020.109096. URL https://www.sciencedirect.com/science/article/pii/S0264127520306316.

[23] Alex Krizhevsky, Ilya Sutskever, and Geoffrey E. Hinton. Imagenet classification with deep convolutional neural networks. *Commun. ACM*, 60(6):84–90, may 2017. ISSN 0001-0782. doi: 10.1145/3065386. URL https://doi.org/10.1145/3065386.

[24] Laith Alzubaidi, Jinglan Zhang, Amjad J Humaidi, Ayad Al-Dujaili, Ye Duan, Omran Al-Shamma, J Santamaría, Mohammed A Fadhel, Muthana Al-Amidie, and Laith Farhan. Review of deep learning: concepts, CNN architectures, challenges, applications, future directions. *Journal of Big Data*, 8(1):53, 2021. ISSN 2196-1115. doi: 10.1186/s40537-021-00444-8. URL https://doi.org/10.1186/s40537-021-00444-8.

[25] Stuart J Russell and Peter Norvig. *Artificial intelligence: a modern approach*. Malaysia; Pearson Education Limited,, 2016.

[26] Yu Qin, Aobo Liu, Hui Guo, Yunong Shen, Peng Wen, Hong Lin, DanDan Xia, Maximilian Voshage, Yun Tian, and Yufeng Zheng. Additive manufacturing of zn-mg alloy porous scaffolds with enhanced osseointegration: In vitro and in vivo studies. *Acta Biomaterialia*, 2022. ISSN 1742-7061. doi: https://doi.org/10.1016/j.actbio.2022.03.055. URL https://www.sciencedirect.com/science/article/pii/S1742706122001945.

[27] Fanman Meng, Kaixu Huang, Hongliang Li, and Qingbo Wu. Class activation map generation by representative class selection and multi-layer feature fusion, 2019. URL https://arxiv.org/abs/1901.07683.

[28] V.S. Deshpande, M.F. Ashby, and N.A. Fleck. Foam topology: bending versus stretching dominated architectures. *Acta Materialia*, 49(6):1035–1040, 2001. ISSN 1359-6454. doi: https://doi.org/10.1016/S1359-6454(00)00379-7. URL https://www.sciencedirect.com/science/article/pii/S1359645400003797.

[29] Jens Bauer, Lucas R. Meza, Tobias A. Schaedler, Ruth Schwaiger, Xiaoyu Zheng, and Lorenzo Valdevit. Nanolattices: An emerging class of mechanical metamaterials. *Advanced Materials*, 29(40):1701850, 2017. doi: https://doi.org/10.1002/adma.201701850. URL https://onlinelibrary.wiley.com/doi/abs/10.1002/adma.201701850.

[30] Yifan Wang, Liuchi Li, Douglas Hofmann, José E Andrade, and Chiara Daraio. Structured fabrics with tunable mechanical properties. *Nature*, 596(7871):238–243, 2021. ISSN 1476-4687. doi: 10.1038/s41586-021-03698-7. URL https://doi.org/10.1038/s41586-021-03698-7.

[31] Benjamin Winter, Benjamin Butz, Christel Dieker, Gerd E Schröder-Turk, Klaus Mecke, and Erdmann Spiecker. Coexistence of both gyroid chiralities in individual butterfly wing scales of callophrys rubi. *Proceedings of the National Academy of Sciences*, 112(42):12911–12916, 2015.

[32] Bodo D Wilts, Kristel Michielsen, Hans De Raedt, and Doekele G Stavenga. Iridescence and spectral filtering of the gyroid-type photonic crystals in parides sesostris wing scales. *Interface Focus*, 2(5):681–687, 2012.

[33] Zakaria Almsherqi, Felix Margadant, and Yuru Deng. A look through 'lens' cubic mitochondria. *Interface focus*, 2(5):539–545, 2012.

[34] Srinivasan Rajagopalan and Richard A Robb. Schwarz meets schwann: design and fabrication of biomorphic and durataxic tissue engineering scaffolds. *Medical image analysis*, 10(5):693–712, 2006.

[35] Muhammad N Yousaf, Benjamin T Houseman, and Milan Mrksich. Using electroactive substrates to pattern the attachment of two different cell populations. *Proceedings of the National Academy of Sciences*, 98(11):5992–5996, 2001.

[36] Jeffrey P Spalazzi, Kathie L Dionisio, Jie Jiang, and Helen H Lu. Osteoblast and chondrocyte interactions during coculture on scaffolds. *IEEE engineering in medicine and biology magazine*, 22(5):27–34, 2003.

[37] Oraib Al-Ketan and Rashid K Abu Al-Rub. Mslattice: A free software for generating uniform and graded lattices based on triply periodic minimal surfaces. *Material Design & Processing Communications*, 3(6): e205, 2021.

[38] Ruggero Gabbrielli, IG Turner, and Chris R Bowen. Development of modelling methods for materials to be used as bone substitutes. In *Key Engineering Materials*, volume 361, pages 903–906. Trans Tech Publ, 2008.

[39] Michael Smith. *ABAQUS/Standard User's Manual, Version 6.9.* Dassault Systèmes Simulia Corp, United States, 2009.

[40] Martín Abadi, Ashish Agarwal, Paul Barham, Eugene Brevdo, Zhifeng Chen, Craig Citro, Greg S. Corrado, Andy Davis, Jeffrey Dean, Matthieu Devin, Sanjay Ghemawat, Ian Goodfellow, Andrew Harp, Geoffrey Irving, Michael Isard, Yangqing Jia, Rafal Jozefowicz, Lukasz Kaiser, Manjunath Kudlur, Josh Levenberg, Dandelion Mané, Rajat Monga, Sherry Moore, Derek Murray, Chris Olah, Mike Schuster, Jonathon Shlens, Benoit Steiner, Ilya Sutskever, Kunal Talwar, Paul Tucker, Vincent Vanhoucke, Vijay Vasudevan, Fernanda Viégas, Oriol Vinyals, Pete Warden, Martin Wattenberg, Martin Wicke, Yuan Yu, and Xiaoqiang Zheng. TensorFlow: Large-scale machine learning on heterogeneous systems, 2015. URL `https://www.tensorflow.org/`. Software available from tensorflow.org.

Checklist

1. For all authors...
   (a) Do the main claims made in the abstract and introduction accurately reflect the paper's contributions and scope? [Yes]
   (b) Did you describe the limitations of your work? [Yes] See Section 3.
   (c) Did you discuss any potential negative societal impacts of your work? [No] We supposed no negative societal impacts.
   (d) Have you read the ethics review guidelines and ensured that your paper conforms to them? [Yes]
2. If you are including theoretical results...
   (a) Did you state the full set of assumptions of all theoretical results? [N/A]
   (b) Did you include complete proofs of all theoretical results? [N/A]
3. If you ran experiments...
   (a) Did you include the code, data, and instructions needed to reproduce the main experimental results (either in the supplemental material or as a URL)? [Yes] See Section A.
   (b) Did you specify all the training details (e.g., data splits, hyperparameters, how they were chosen)? [Yes] See Section A.1.5.
   (c) Did you report error bars (e.g., with respect to the random seed after running experiments multiple times)? [N/A]
   (d) Did you include the total amount of compute and the type of resources used (e.g., type of GPUs, internal cluster, or cloud provider)? [Yes] See Section A.1.5.
4. If you are using existing assets (e.g., code, data, models) or curating/releasing new assets...
   (a) If your work uses existing assets, did you cite the creators? [Yes]
   (b) Did you mention the license of the assets? [N/A]
   (c) Did you include any new assets either in the supplemental material or as a URL? [Yes] See Section A and `https://github.com/DeepHeisenberg/GAD-MALL`.
   (d) Did you discuss whether and how consent was obtained from people whose data you're using/curating? [N/A] All data was generated by ourselves.
   (e) Did you discuss whether the data you are using/curating contains personally identifiable information or offensive content? [N/A] We supposed no personally identifiable information or offensive content.
5. If you used crowdsourcing or conducted research with human subjects...
   (a) Did you include the full text of instructions given to participants and screenshots, if applicable? [N/A]
   (b) Did you describe any potential participant risks, with links to Institutional Review Board (IRB) approvals, if applicable? [N/A]
   (c) Did you include the estimated hourly wage paid to participants and the total amount spent on participant compensation? [N/A]

A Appendix

A.1 Methods

A.1.1 TPMS structure generation

Triply periodic minimal surfaces (TPMS) and related structures are widespread in natural biological systems [31, 32, 33]. TPMS is considered to be the ideal geometric shape to describe the biological form of the human skeleton [34]. Numerous studies have shown that the curved surfaces of TPMS contribute to enhanced plasma membrane elongation during cell crawling and spreading [35, 36]. In this study, we adopted the Gyroid minimal surface structure, which is a member of the TMPS family. In addition to these above-mentioned advantages of TMPS, the unique helical surface structure of the Gyroid unit makes the force distribution more uniform, leading to its excellent mechanical properties. The equation of Gyroid surface is as follows [37]:

$$\phi_G \equiv \sin X \cos Y + \sin Y \cos Z + \sin Z \cos X = c \tag{2}$$

The equation $\phi(X, Y, Z)$ defines a surface evaluated at the isovalue (i.e., level-set constant) c and has a topology similar to that of a minimal surface. $X \;\; 2\alpha\pi x$, $Y \;\; 2\beta\pi y$, $Z \;\; 2\gamma\pi z$, α, β, and γ are constants related to the unit cell size in the x, y and z directions, respectively. In this work, we created the Gyroid lattice based on the minimal surface by considering one of the volumes divided by the surface as the solid domain and the other as the void domain. This was done by considering the volume bounded by the minimal surface such that $\phi(X, Y, Z) \;\; c$ to create a solid-network lattice. The porosity of Gyroid lattices can be graded by varying the value of the level-set constant c spatially in the Cartesian space depending on a certain function or tabulated data such that [38]:

$$\phi_G > c(x, y, z) \tag{3}$$

To achieve a smooth transition between units on the edge (Section A.3, Fig. 11), we describe the iso-value as a linear function along one of the Cartesian coordinates such that $c \;\; Ax \; B$ where A and B are constants. This smooth transition is a prerequisite for representing the actual geometry shape using a porosity matrix.

The scaffold contains 27 Gyroid sub-units in total, arranged as a $3 \times 3 \times 3$ cubic. The geometry of the scaffold is controlled by the $3 \times 3 \times 3$ porosity matrix. The porosity c of each sub-unit can take discrete values from 20 to 80 %, with the increment of 10 %.

A.1.2 Dataset generation

The unlabeled dataset consisted of 18000 data points and was generated for the training of the 3D-CAE. In principle, the porosity of a sub-unit can take any value from 0 to 1. Therefore, the possible arrangement is infinite. To simplify the problem, we allow the scaffold's porosity takes discrete values from 10 to 80 % with an interval of 10% (more detail is described in the TMPS structure generation section). Nevertheless, there are still 7^{27} possible combinations in the design space. Three thousand matrices of various porosities were generated at each interval. For each interval, there are three kinds of symmetry in the database (Section A.3): central, vertical, horizontal, and random arrangement. The porosity matrices also have three kinds: $2 \times 2 \times 2$, $3 \times 3 \times 3$ and $4 \times 4 \times 4$, which then all expand to a $12 \times 12 \times 12$ matrix (Section A.3, Fig. 12(B)). In such a way, our 3D-CAE can generate three different kinds of porosity matrices. This study chose the $3 \times 3 \times 3$ arrangement to balance structural complexity and computational efficiency; nonetheless, our GAD-MALL can handle three different scaffold arrangements in principle.

For the labeled dataset, the labels (the elastic modulus (E) and yield strength (Y) of the corresponding scaffolds) were computed by the finite element method (FEM), whose accuracy was verified through careful calibration with experimental data. It was confirmed that the deviations between experiment and simulation were less than 10% (see Section A.3).

A.1.3 3D printing and compression tests

The performance of powder shows much influence on formation quality of 3D-printed products. Spherical Ti6Al4V (Ti) powders with few satellite particles with good flowability were applied for

3D printing. The powder sizes of D10, D50 and D90 in statistics were 23.9, 37.8 and 58.5 μm respectively. The Ti scaffolds with the size of 6 × 6 × 6 mm were additively manufactured by laser powder bed fusion (LPBF) process using an EOS M290 machine in this work. The processing chamber was filled with argon gas to avoid harmful reactions. The key LPBF parameters used were as follows: the laser power of 280 W, the laser scanning speed of 1200 mm/s, and the layer thickness of 30 μm. After heat treatment at a temperature of 800 °C for 2 hours and cooled in a furnace, the Ti scaffolds were surface treated by sandblasting. The Ti6Al4V sand with an average grain size of 106 μm was used in the sandblasting process. Uniformly blasted the outer surface of the Ti scaffolds to remove the adhered powder particles, with a pressure of 0.6 MPa at the outlet of the spray gun. The relative density of the composing struts in the Ti scaffolds was greater than 99.5%.

The pure zinc (Zn) powder sizes of D10, D50 and D90 in statistics were 10.2, 19.6 and 39.4 μm respectively. The Zn scaffolds of 6 × 6 × 6 mm were processed using a BLT S210 machine. The processing chamber was filled with argon gas and a gas circulation system was employed to inhibit the negative effect of vaporization during the LPBF process. The Zn scaffolds were fabricated with a laser power of 40 W, a laser scanning speed of 500 mm/s, and a layer thickness of 0.03 mm. Chemical etching with 5% nitric acid and 5% hydrochloric acid (RT, 2 min) was applied to remove the adhered powder particles, and the relative density of the composing struts in Zn scaffolds reached 98.5%.

Compression tests were conducted using an Instron machine (10 kN load cell) at a crosshead speed of 1mm/min at room temperature. The compress direction was parallel with the building direction. Three replicas were manufactured in order to ensure reproducibility.

A.1.4 Numerical simulation parameters

We performed the compression simulation on a CPU (Intel Xeon Gold 6226R Processor) with 32-Core and 64-Thread using ABAQUS/Explicit software [39]. The FEM was based on the same rigid-cylinder and deformable-implant-structure model. The material was homogeneous, and the Poisson's ratio was 0.25. The E was set to 5 GPa and the Y to 120 MPa based on the compression experiments of the block pure Zn prepared by LPBF. Ductile damage was used to simulate the plastic deformation to the failure stage. Fracture strain was set as 0.03, and the effects of triaxiality deviation and strain rate were neglected. We extracted displacements and forces in post-processing and then converted them to strains and stresses, respectively.

A.1.5 Machine learning algorithms

The 3D-CAE consisted of an encoder and decoder. The encoder was composed of 3 3D convolutional layers (Conv3D). The input size was (12, 12, 12, 1). The first, second, third, and fourth layers contained 60, 30, and 15 filters. Three max-pooling layers between the convolutional layers were responsible for the down-sampling. For example, one max pooling layer reduced the size of Conv3D from (12, 12, 12) to (6, 6, 6), shrinking each (2, 2, 2) box down to (1, 1, 1), and taking the maximum as its value. The size of the final layer is (3, 3, 3, 15). Another max-pooling reduced it to the hidden representation (1, 1, 1, x), where x represents the dimension. The decoder is of the same Conv3D architecture, but with up-sampling, converting the hidden feature (1, 1, 1, x) back to (12, 12, 12, 1). Reconstruction loss was the mean square error (MSE) between input and output.

The 3D-CNN model consisted of 3 convolutional layers. The first, second, and third layers contain 8, 4, and 2 filters, respectively; three max-pooling layers are located behind each convolutional layer. Finally, before reaching the output node, the last layer was flattened into 1048 neurons, followed by a series of fully connected layers (128, 64, 32). The activation function was the exponential linear unit. Moreover, the loss function was the mean square error. The program was written using Keras and Tensorflow [40]. We trained the 3D-CAE and 3D-CNNs using a GPU (NVIDIA GeForce RTX 3080) with 10GB of memory. The training results and performance evaluation of both the 3D-CAE and 3D-CNNs can be found in Section A.2.

A.2 Model performance evaluation

The task in this study can be mathematically formulated as follows:

$$
\begin{aligned}
&\text{Find } x \in H\\
&\text{To the mapping } f : H \longrightarrow Y \text{ and } g : H \longrightarrow E\\
&\text{Such that } x \;\; argmax_{x\in H}(f(x)) \text{ and } g(x) \;\; E_{target}\\
&\text{Under the constraint: weight \;\; fixed constant}
\end{aligned}
\tag{4}
$$

H is the scaffold design space; f and g are the mappings of scaffold design to its corresponding Y and E. Fig. 6 shows a visualization of the exploration path.

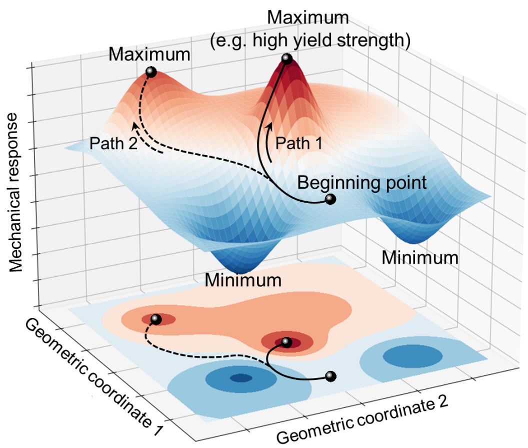

Figure 6: **Representation of the constrained multi-objective optimization task in this study.** The contour surface represents the arrangement with equal E. The task is to find the maximum yield point on this surface.

Fig. 7 shows the training history of 3D-CAE with eight latent dimensions. The loss quickly dropped to near zero after 60 epochs. The histogram (inlet) shows that the loss of 4-dimension latent space was high, while sampling from the 16-dimension was time-consuming. 8-dimension reached a balance between loss and efficiency.

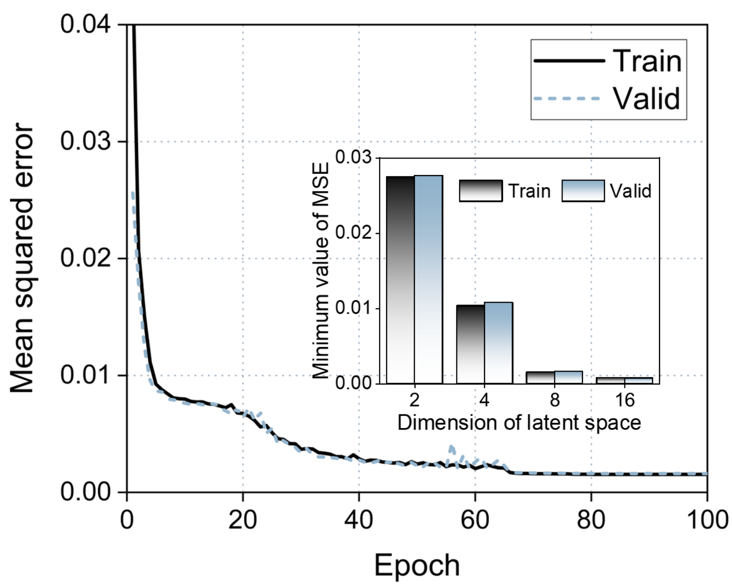

Figure 7: **Training of 3D-CAE.** Training history of 3D-CAE. The loss reaches almost zero after 60 epochs; inlet shows the histogram of the loss v.s. the latent space dimension.

Fig. 8 and 9 demonstrate the performance evaluation of 3D-CNNs (for the E and Y) on the Ti and Zn test dataset. Both 3D-CNNs show high accuracy in the regression tasks (R^2 ratio 0.98) at each active learning iteration. The test dataset was uniformly sampled from the labelled dataset.

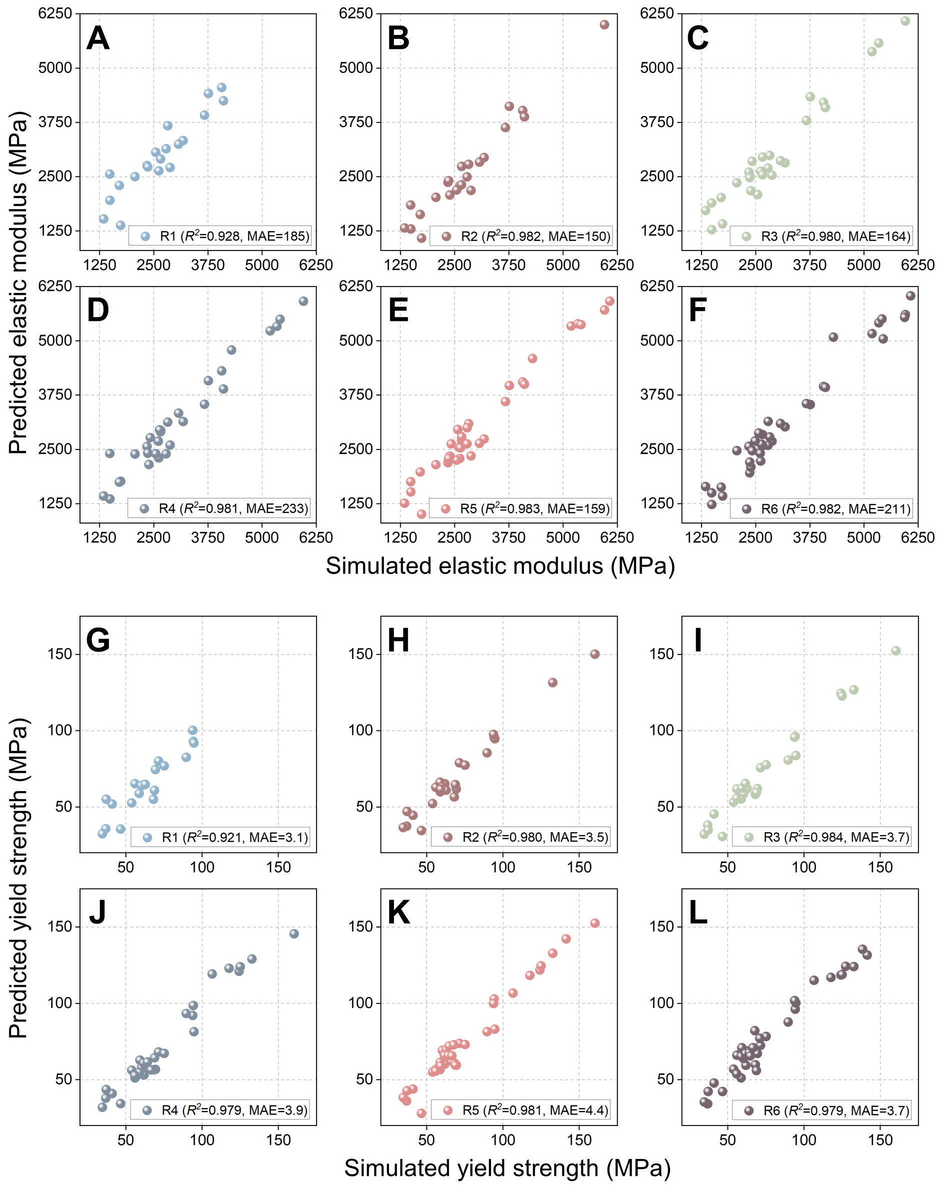

Figure 8: **Performance evaluation of 3D-CNNs on the Ti test dataset.** (**A** to **L**) show the R^2 and mean average error (MAE) of 3D-CNNs from round 1 to 6, (**A** to **F**) refer to the E and (**G** to **L**) refer to the Y.

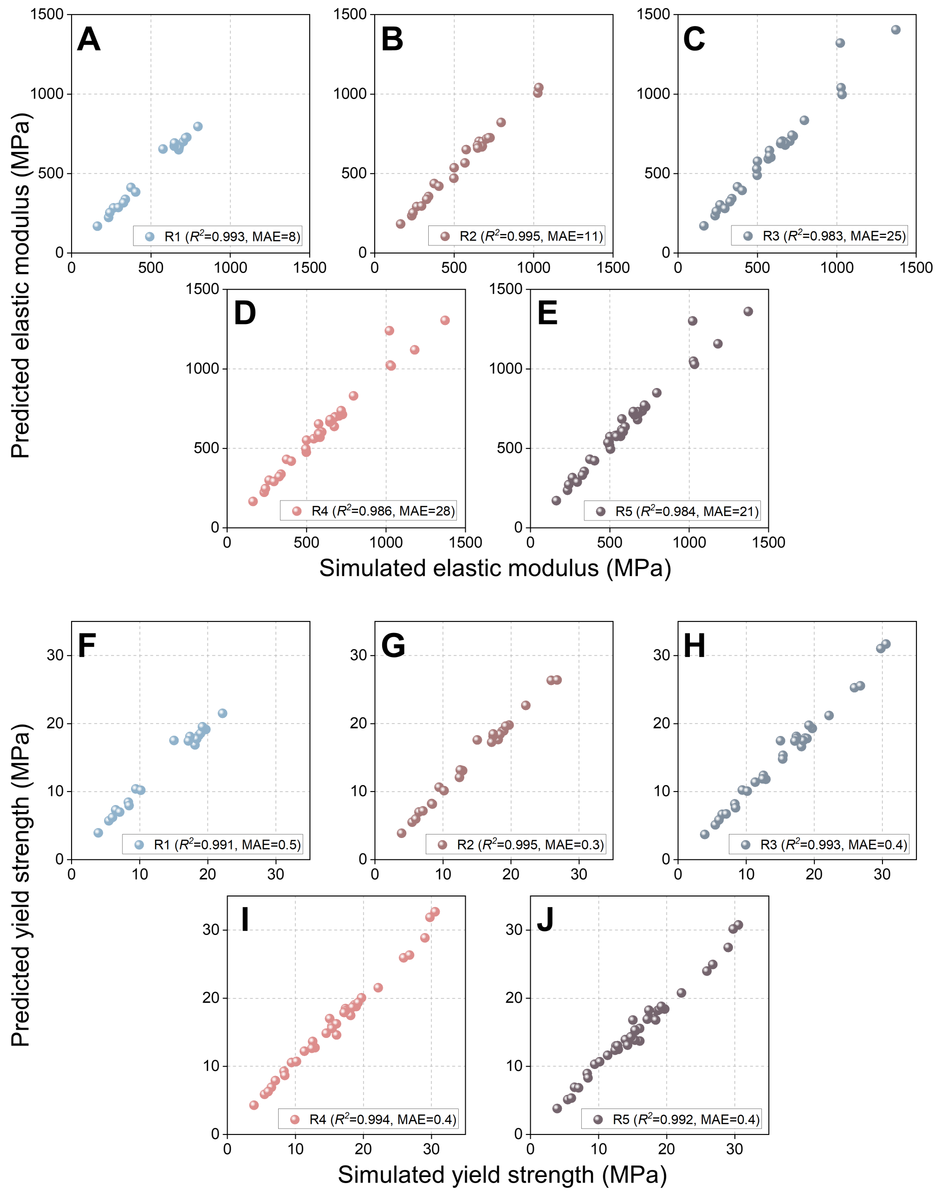

Figure 9: **Performance evaluation of 3D-CNNs on the Zn testing dataset.** (**A** to **J**) show the R^2 and mean average error of 3D-CNNs from round 1 to 5, (**A** to **E**) refer to the E and (**F** to **J**) refer to the Y.

The Gaussian mixture model (GMM) was used to estimate the density in the latent z space (i.e., the marginal posterior $q_\phi(z)$). GMM is a density estimation model that uses a mixture of a finite number of Gaussian distributions with unknown mean and covariance to fit the data points. The number of Gaussian distributions is usually determined via the empirical elbow method. The elbow method is a heuristic used in determining the Pareto fronts in multi-objective optimization, in this case, it was used to determine the potential optimal number of Gaussian). As shown in Fig. 10, the average negative log-likelihood was plotted as a function of the number of Gaussian and we selected 4 as it represents the 'elbow' of the curve.

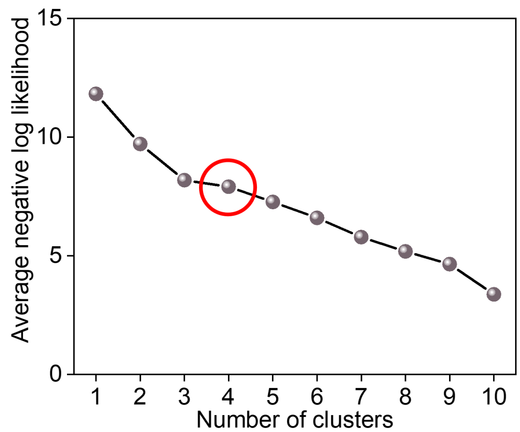

Figure 10: **The average negative log-likelihood versus the number of clusters in the GMM.**

Table 1 and 2 contain the result of each learning iteration for the Ti and Zn cubic scaffolds, respectively.

Table 1: The Ti cubic scaffolds - Mean and standard deviation of the E and Y at each iteration

	E2500 Task			E5000 Task		
Iteration	**Elastic modulus (MPa)**	**Yield strength (MPa)**	**Porosity (%)**	**Elastic modulus (MPa)**	**Yield strength (MPa)**	**Porosity (%)**
1	2311 ± 73	57.7 ± 3.3	74.1 ± 0.3	6226 ± 408	139.7 ± 11.8	57.3 ± 1.7
2	2684 ± 69	62.6 ± 3.1	71.8 ± 0.7	5789 ± 142	136.6 ± 5.3	57.3 ± 0.3
3	2423 ± 59	65.1 ± 5.3	70.6 ± 1.2	5526 ± 122	124.8 ± 6.8	58.5 ± 0.3
4	2570 ± 47	66.6 ± 3.9	70.3 ± 0.7	5072 ± 147	119.1 ± 5.8	60.4 ± 0.6
5	2686 ± 156	69.4 ± 5.2	69.6 ± 1.3	5271 ± 81	129.4 ± 9.8	57.0 ± 1.3
6	2566 ± 47	70.0 ± 1.7	70.1 ± 0.3	5059 ± 128	136.0 ± 5.9	57.5 ± 0.9

Table 2: The Zn cubic scaffolds - Mean and standard deviation of the E and Y at each iteration

	E500 Task			E1000 Task		
Iteration	**Elastic modulus (MPa)**	**Yield strength (MPa)**	**Porosity (%)**	**Elastic modulus (MPa)**	**Yield strength (MPa)**	**Porosity (%)**
1	546 ± 52	12.9 ± 0.8	57.9 ± 0.5	1024 ± 22	26.2 ± 0.7	45.1 ± 0.2
2	508 ± 19	12.1 ± 0.6	59.1 ± 0.8	1297 ± 85	32.1 ± 1.3	38.0 ± 0.5
3	568 ± 34	15.2 ± 0.9	56.7 ± 0.9	1123 ± 71	28.8 ± 0.9	41.9 ± 1.3
4	555 ± 31	14.8 ± 0.7	56.0 ± 1.1	1024 ± 27	29.4 ± 0.3	43.2 ± 0.5
5	515 ± 16	14.2 ± 0.7	58.9 ± 0.2	965 ± 18	28.8 ± 0.5	43.7 ± 0.1

A.3 Data generation

Fig. 11 shows the schematic for the smooth transition between units with different porosity.

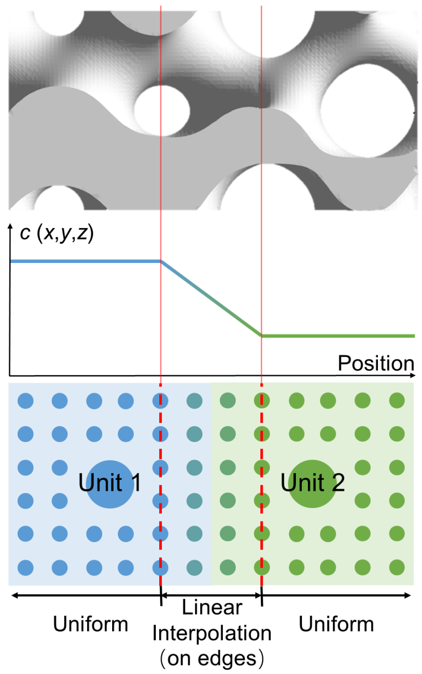

Figure 11: **The schematic for the smooth transition between units with different porosity.**

Fig. 12(A and B) show the schematics for unlabelled scaffold preparation. Fig. 12(C to H) shows the simulation and experimental data of two randomly selected cubic scaffolds. ABAQUS/Explicit software was used for compression simulation [39].

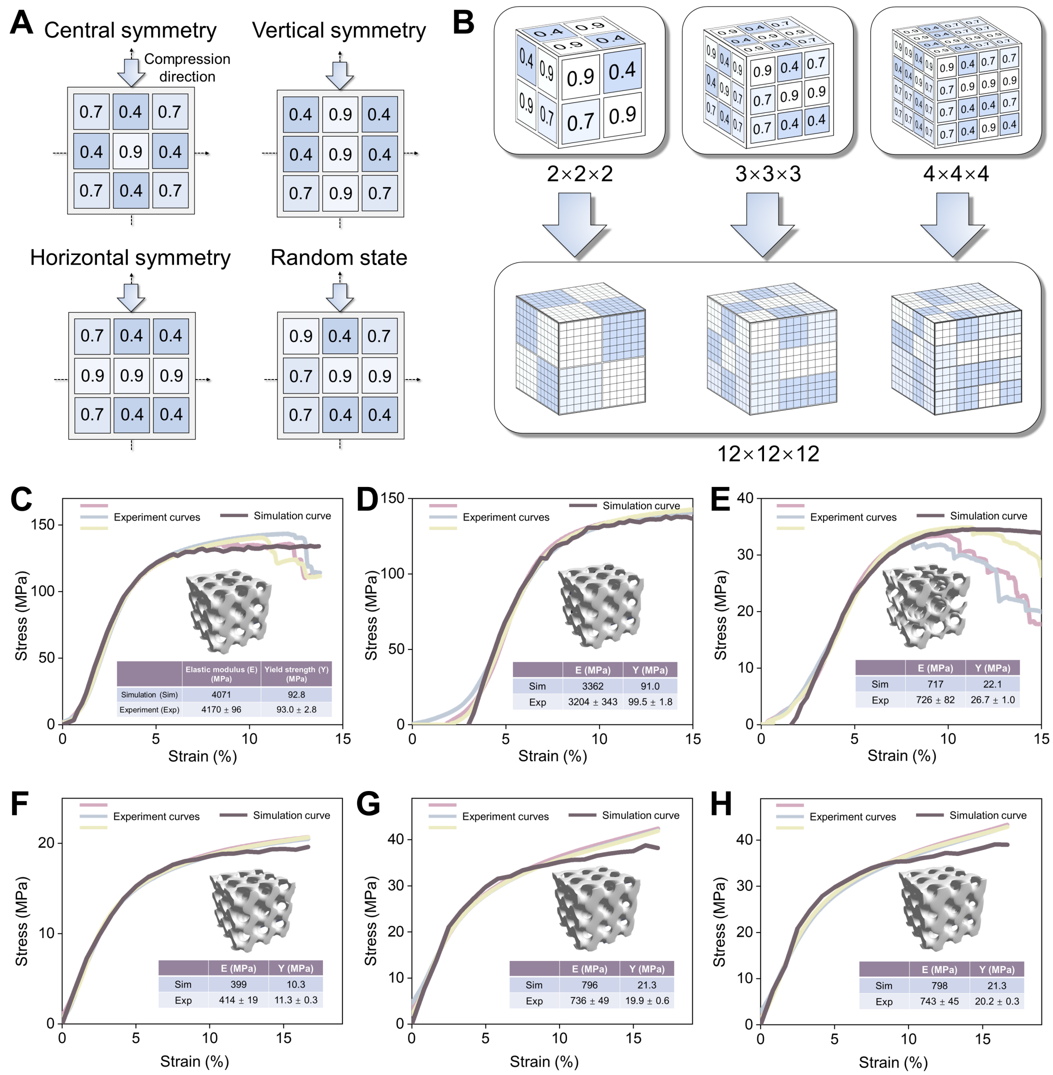

Figure 12: **Data generation and simulation calibration.** (**A**) The porosity matrix database contains three symmetries and one random arrangement. (**B**) Three kinds of porosity matrices: $2 \times 2 \times 2$, $3 \times 3 \times 3$ and $4 \times 4 \times 4$, which can all expand to a $12 \times 12 \times 12$ matrix. The $3 \times 3 \times 3$ arrangement was chosen to balance structural complexity and computational efficiency. (**C** to **H**) The FEM simulation agrees with experimental observations. Three replicas were tested in order to ensure reproducibility. The error of the E and Y between FEM simulation and experimental results is less than 10%. (C to E) refer to 3 Ti scaffolds with random shapes, and (F to H) refer to 3 Zn scaffolds with random shapes. (C to H) All stress-strain curves are adjusted in the x-axis direction to make them overlap.

A.4 FEM analysis of cubic scaffolds

This section discusses the detailed FEM analysis of ML design cubic scaffolds from E2500 (Ti), E5000 (Ti), and E1000 (Zn) tasks.

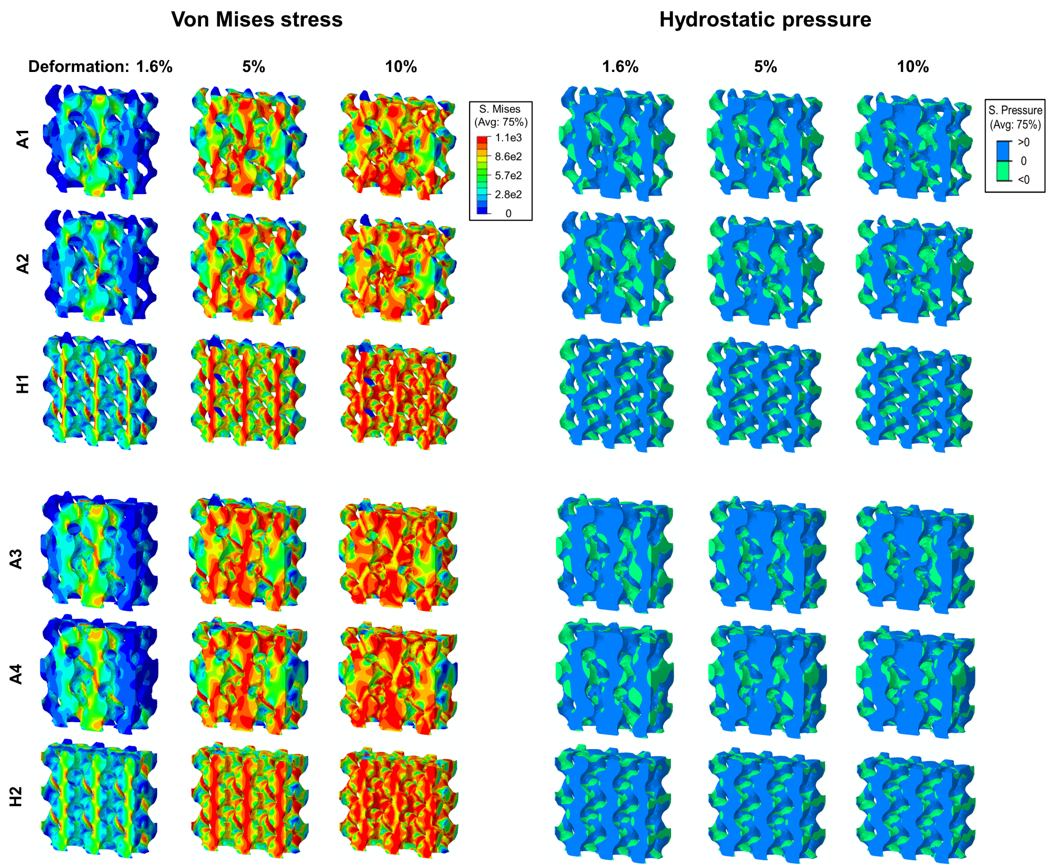

Figure 13: **FEM analysis of the Ti cubic scaffolds.** Numerical compression analysis of Von-Mises stress and hydrostatic pressure under 1.6%, 5%, 10% deformation. The cross-section view of ML designs (A1-A4) and expert designs (H1 and H2) is plotted.

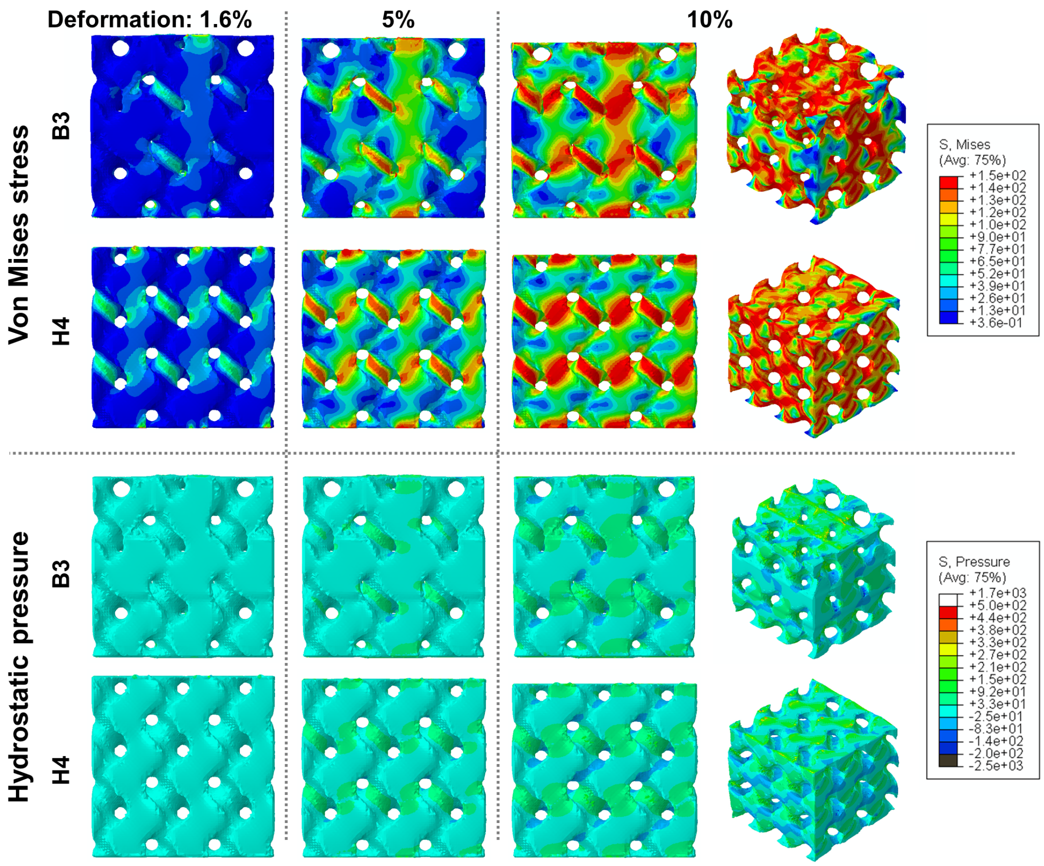

Figure 14: **FEM analysis of the Zn cubic scaffolds.** Numerical compression analysis of Von-Mises stress and hydrostatic pressure under 1.6%, 5%, 10% deformation. The front and orthographic views of ML design (B3) and expert design (H4) are plotted.

A.5 Experimental characterization of cubic-shaped scaffolds

Table 3: Experimental result of ML design and expert design Ti cubic scaffold. A1(2) and A3(4) represent the best candidates for E2500 and E5000 tasks, respectively. Expert design (uniform) H1 and H2 are the reference scaffolds of E2500 and E5000

	A1	**A2**	**H1**	**A3**	**A4**	**H2**
Elastic modulus (MPa)	2527 ± 87	2649 ± 195	2627 ± 154	5169 ± 422	4947 ± 450	4903 ± 303
Yield strength (MPa)	74.8 ± 2.2	73.4 ± 1.9	60.0 ± 1.1	147.6 ± 4.2	147.2 ± 2.3	119.8 ± 8.6
Porosity (%)	69.3 ± 0.3	69.1 ± 0.1	73.0 ± 0.2	57.5 ± 0.3	55.6 ± 0.1	60.8 ± 0.3

Table 4: Experimental result of ML design and expert design Zn cubic scaffolds. B1(2) and B3(4) represent the best candidates from E500 tasks and E1000, respectively. H3(4) are the reference scaffolds (uniform porosity) of E500 and E1000. B3 scaffold shows superior performance over the gold criteria H4 scaffold

	B1	**B2**	**H3**	**B3**	**B4**	**H4**
Elastic modulus (MPa)	484 ± 17	510 ± 28	510 ± 28	1066 ± 35	1012 ± 22	975 ± 19
Yield strength (MPa)	13.0 ± 0.6	12.7 ± 0.3	12.9 ± 0.5	26.4 ± 0.7	21.8 ± 0.7	21.7 ± 1.8
Porosity (%)	56.5 ± 0.5	56.8 ± 0.2	55.8 ± 0.1	35.4 ± 0.2	38.6 ± 0.1	39.3 ± 0.4

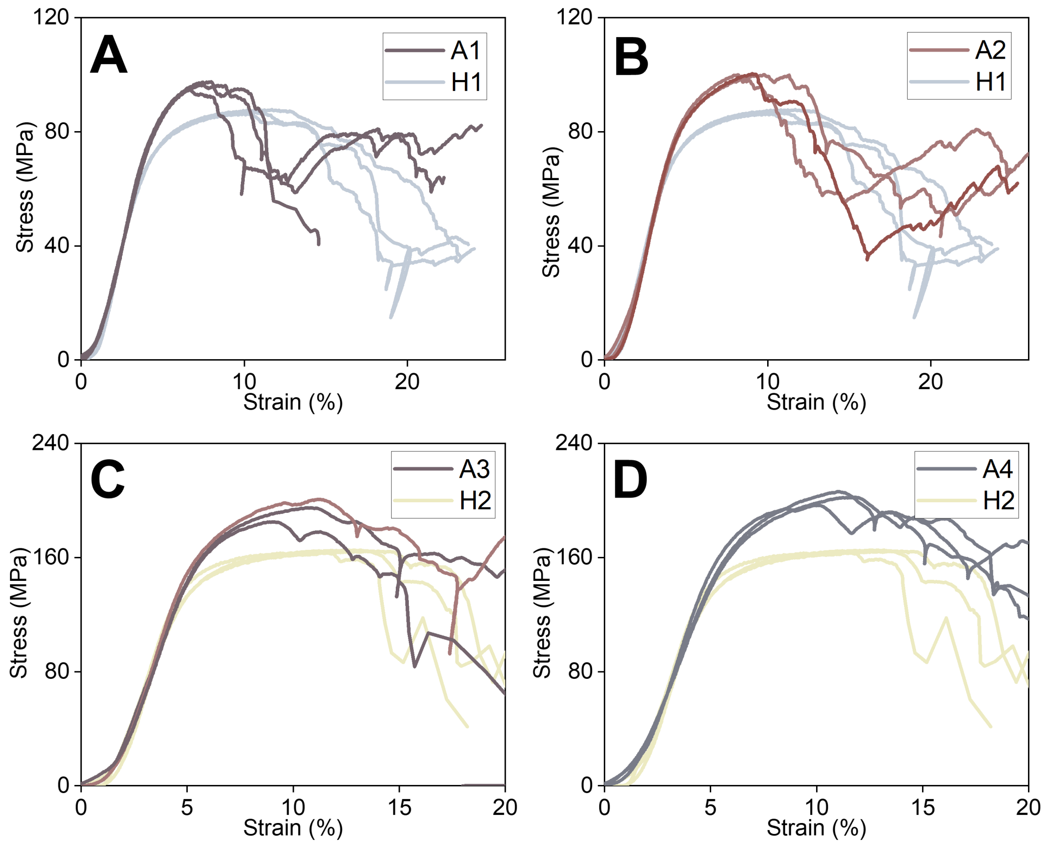

Figure 15: **Compression test curves of the Ti cubic scaffolds.** ML designs (A1-A4) and expert designs (H1 and H2). Three replicas were tested in order to ensure reproducibility. In each figure, all stress-strain curves are adjusted in the x-axis direction to make them overlap.

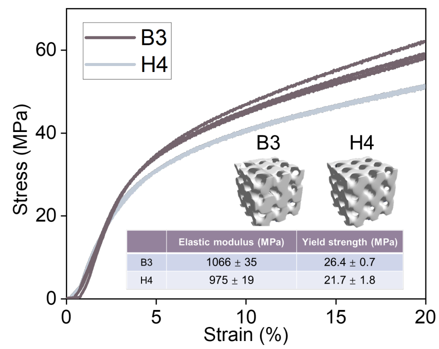

Figure 16: **Experimental strain-stress curves of the Zn cubic scaffolds.** ML design (B3) and expert design (H4). Three replicas were tested in order to ensure reproducibility. In each figure, all stress-strain curves are adjusted in the x-axis direction to make them overlap.

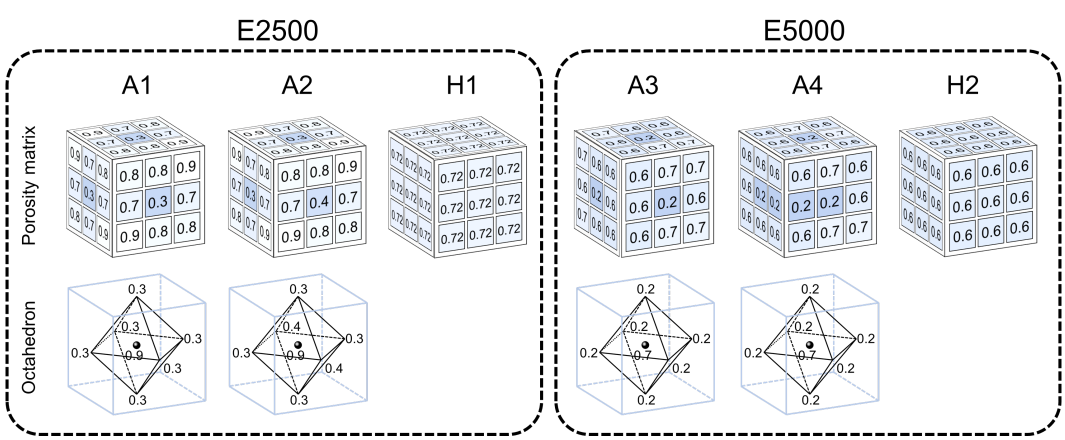

Figure 17: **The porosity matrices and 'face-centered' lattice structures of the Ti cubic scaffolds.** The porosity matrices of ML designs (A1-A4) and expert designs (H1 and H2). The 'face-centered' lattice structures of ML designs (A1-A4).

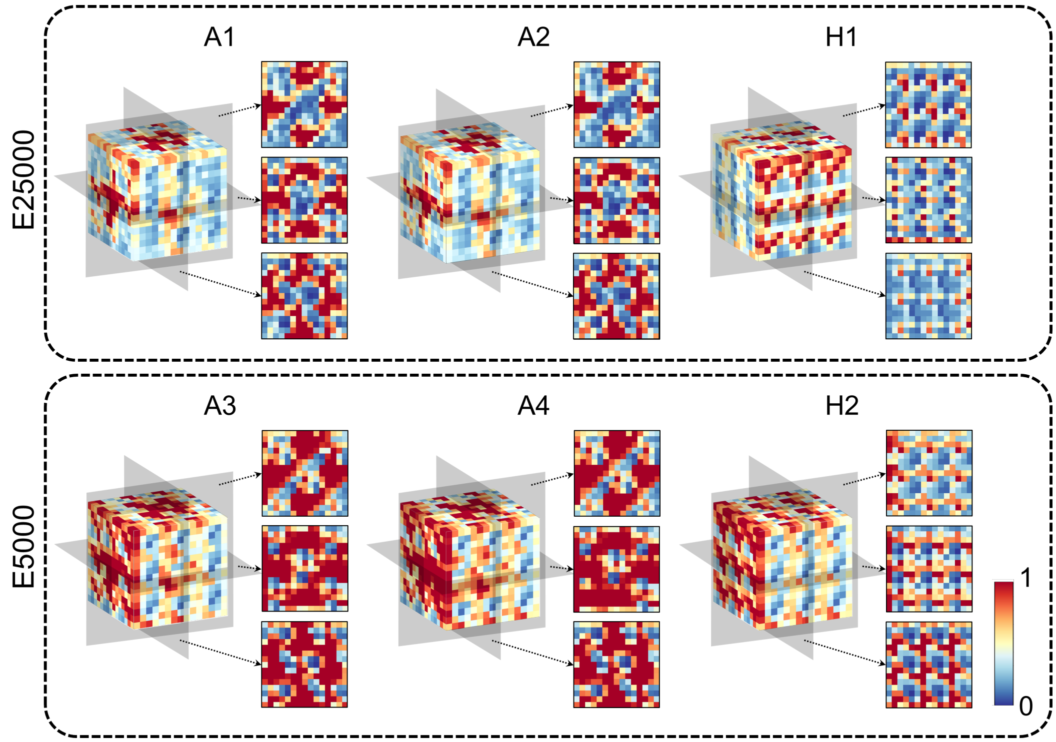

Figure 18: **Regression activation map of the Ti cubic scaffolds.** The x-z, x-y, and y-z cross sections of the RAM of ML designs (A1-A4) and expert designs (H1 and H2).

A.6 Irregular-shaped scaffolds for bone implants

Fig. 19 shows the design workflow for an irregular-shaped scaffold. We used a $3 \times 3 \times 9$ raw structure as the starting point. The sub-unit is the ML-designed cubic scaffold. Overall, the whole structure consists of $9 \times 9 \times 27$ Gyroid units. The scaffold structure was then caved out of the raw materials with the shape matching that of the bones.

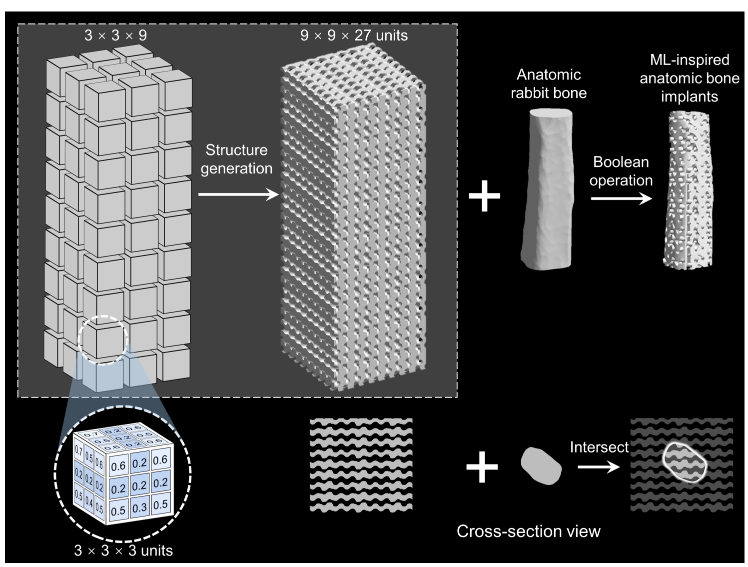

Figure 19: **Pipeline for irregular-shaped scaffold design.** We used the $3 \times 3 \times 9$ raw structure as the starting point, with each sub-unit representing the ML-designed cubic scaffold. The bone-shaped scaffold was then caved out of the raw structure.

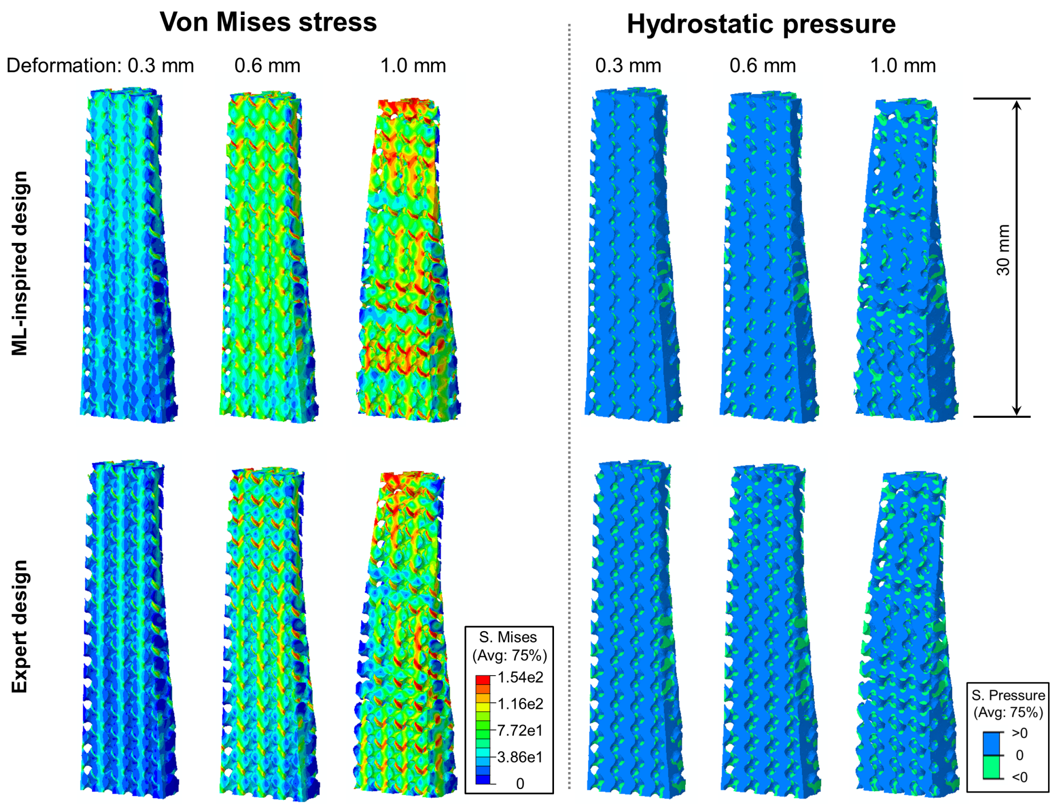

Figure 20: **FEM analysis of the anatomic bone implant.** Numerical compression analysis of Von-Mises stress and hydrostatic pressure under 0.3, 0.6, 1.0 mm deformation. The cross-section view of ML-inspired design and expert design is plotted.